Physical Education, Health and Social Sciences

https://journal-of-social-education.org

E-ISSN: 2958-5996
P-ISSN: 2958-5988

Optimization and kinetics for Se^{4+}/TiO_2 enhanced photocatalytic performance against Polyethylene

Zaib-un-Nisa[a*]

[a*]Minhaj University Lahore Email: Zaibunnisa.che@mul.edu.pk
*Corresponding authors: Zaib-un-Nisa, E-mail address: zaibunnisa.che@mul.edu.pk

DOI: https://doi.org/10.63163/jpehss.v3i2.424

Abstract

Plastic pollution poses a significant environmental threat, with polyethylene (PE) being one of the most persistent polymers. Conventional recycling methods have limitations, necessitating innovative degradation approaches. In this study, Se^{4+}-doped TiO_2 (TSe) nanocatalysts were synthesized via the sol-gel method with varying selenium concentrations (0.1–1 w/w%) to enhance photocatalytic performance under visible light. Characterization using XRD, Raman, BET, SEM, FTIR, PL, and UV/Vis spectroscopy confirmed successful doping, structural modifications, and a reduced bandgap (minimum 2.7 eV). Photocatalytic degradation of PE was evaluated, revealing that TSe0.5 exhibited optimal performance with a degradation efficiency of 92.2% and a recyclability of 10 cycles at 52.76% efficiency. Response surface methodology (RSM) was applied to optimize pH, temperature, and catalyst concentration, demonstrating a significant impact on degradation efficiency. The enhanced photocatalytic activity was attributed to Se^{4+} incorporation, leading to improved charge carrier separation, increased surface area, and extended visible light absorption. These findings highlight the potential of Se-doped TiO_2 nanocatalysts for efficient and sustainable PE degradation

Keywords: Se doped TiO_2, Sol-Gel, Nanocatalysts, Photocatalytic activity, polyethylene, RSM optimization.

Introduction

Due to the widespread use of plastics in packaging, food storage, medicine, apparel, automobile materials, toys, personal care products, and other applications, plastic pollution has become a global problem. The United States Environmental Protection Agency (US EPA) stated that about 200 tonnes of plastic are produced each year [1]. According to UNEP survey conducted in the early 2000s, we produced more plastic waste in one decade than we had in the preceding forty years [2]. The most common types of plastic were nylon polymers, polyethylene, polystyrene, polypropylene, fluorocarbon polymers, polyethylene terephthalate, polyurethane and polyvinyl chloride, and acrylonitrile butadiene styrene [3, 4]. In everyday market, polyethylene products with low density (LDPE) and high density (HDPE) have the highest commercial value [5]. In addition, microplastics are divided into primary and secondary MPs according to the way they are released. Secondary MPs are made from big plastic objects that break down into smaller particles when exposed to the environment, whereas primary MPs are discharged into the environment as tiny particles [6]. A vast variety of living things may experience blockage and inflammation in several organs due to MP accumulation in the gut. There is a possibility that those who deal with synthetic textiles have increased mortality from lung cancer or gastric and esophageal malignancies [7-10]. Additionally, MPs alter gene expression, trigger genotoxicity, and elicit immunological responses [10-12]. Consequently, the environmental effect of plastic trash must be reduced by proper management. The waste

plastic is very energy-dense, recyclable, and capable of being recovered [13]. Not much research has been done on the deterioration of plastics. For example, Zalerion maritimum a specie of fungus has been shown to bio/photocatalyze the degradation of polyethylene polymers [14]. Other materials that have been studied include titania nanotubes [15], ZnO [16], N-doped TiO_2 [17-19], and Pt/ZnO [20, 21]. However, the emphasis has been on traditional methods for breaking down polyethylene polymers.

Therefore, to lessen the harm that plastic trash causes to the environment, proper management is required and researchers have focused a lot of emphasis on selenium-based catalysts since they are reasonably inexpensive and offer improved catalytic systems [22, 23]. The coupling of dynamic catalysts based on selenium with a high semi-metallic dispersion leads to controlled stability, activity and resistance. A number of techniques, including physically combining with other semiconductors and doping TiO_2 with non-metal and transition metal elements [24-27], have been proposed to increase the absorption of visible light by TiO_2 and its photoactivity. This goal can be achieved by incorporating the metalloid into the structure of a crystalline precursor oxide [28].

Numerous dopants have been used to dope TiO_2, including Ag, Fe, S, C, B, N, halogen atoms, Si, Se, and other elements [29-34]. The non-metal elements N, S, Se, and Si appear to be the most preferred dopants for TiO_2. This is due to its low ionisation energy, stability, and ionic radius being comparable to that of oxygen, all of which raise the possibility that oxygen will be replaced within the network. Studies shows that creating a Si-O-Ti link by Si doping, the photocurrent density was greatly increased and the transmission of photogenerated electrons was speed up [35, 36].

Se-doped TiO_2 exhibited increased photocatalytic activity when a suitable amount of Se was utilised. Selenium (Se) is a metal that belongs to the same group as oxygen (O) and According to studies, selenium anions exist as (Se^{2-}) and cations as (Se4+, Se6+). These features may cause new electronic states to enter the TiO2 band gap [37, 38]. Methods for inserting Se ions into TiO_2 include ammonolysis, sol-gel, hydrothermal or solvothermal procedures, sputtering, and ion implantation [39, 40]. The sol-gel method is the most widely used of them [41]. Using this approach, materials with regulated porosity and form at the nanoscale length may be produced [42]. However, for effective doping using the sol-gel approach, a high calcination temperature and a longer time are needed for the sol to turn into a gel. The calcination process at high temperatures causes a reduction of surface area. Low calcination temperature and short ageing time have been used with the sol-gel technique to produce undoped and doped TiO_2 [43-45]. Zhang et al. developed the SeO_2/TiO_2 nanocomposites in order to effectively inhibit the recombination of electron-hole pairs and enhance the wavelength of absorption to visible light. Because to its ionic state of Se^{4+}, se has a low band gap of 2.0 eV [46, 47]. A smaller band gap energy and an expansion of the absorption to the visible light spectrum were the results of adding Se to anatase TiO_2 using a variety of methods [48].

Consequently, a significant enhancement in photocatalytic activity was achieved under visible light. In order to reduce the band gap and improve the photocatalytic activity under visible light irradiation, higher quantities of Se should be doped into TiO_2.

Taking into account earlier research in this area, we note that selenium cation in different concentrations has not yet been extensively employed in TiO_2 doping procedures. Se-doped TiO_2 has been used in very few investigations, but its degrading efficiency is studied against dye or pesticides mostly.

In this research paper high purity anatase TiO_2, with small particles and a large surface area, doped with variable w/w ratio of Se (TSe0.1, TSe0.5, and TSe1) was synthesised using the integrated sol-gel process with a short crystallisation time (2h) and high temperature (450 °C). The as synthesized nanoparticles ability to degrade LDPE under visible light irradiation by photocatalysis was assessed. RSM optimised the temperature, pH, and catalyst concentration. To the best of our knowledge, no prior investigations on the degradation of polyethylene have been conducted using Se/TiO_2 along with RSM optimization.

Reagents and Materials

Titanium (IV) isopropoxide (TTIP), Selenium dioxide (SeO_2), hydrochloric acid (HCl), 2-propanol, ethanol (98%) was purchased from Sigma Aldrich and utilised without further purification, whereas low density polyethylene was bought from a Lahore local market.

Preparation of Se^{4+}/TiO_2

Synthesis of TiO_2 and Se^{4+} was done by sol-gel method as mentioned in literature [49]. In first step, 5 mL TTIP was added into 50 mL of 2-propanol and stirred for 3 hours. Selenium dioxide was added to water in different concentrations (0.1, 0.5, and 1 w/w% to TiO_2). After vigorous stirring, the former solution was added dropwise into the SeO_2 solution and allowed the reaction for further stirring of 24 h making sure that the gel forms. This gel was then dried at 80 °C followed by calcination for 2 h at 450 °C this temperature was attained by gradually increasing at a rate of 2 °C/min. The final product is grounded in an agate pestle mortar into fine powder.

Characterization methods

X-ray diffractometer (Bruker D8 Advance DIFFRAC.EVA) with monochromatized Cu-Kα radiation (λ = 1:541 Å) was used for XRD. The patterns were captured in 2θ spanning from 20° to 70° at room temperature using a scanning step of 0.05/s. The average size of the crystallites was calculated by Debye Scherrer formula as mentioned in equation 1.

$$\tau = \frac{K\,\lambda}{\beta\,\mathrm{Cos}\theta} \qquad (1)$$

Here, λ is the X-ray wavelength of the Cu-kα radiation, and β is the full-width half-maximum resulting from a small crystallite size. The mean size of the ordered and crystalline domains, τ, may be less or equal to the particle size, whereas the dimensionless component K has a value close to unity. The size and form of NPs were examined using VEGA3 TESCAN scanning electron microscopy. (QUANTAX EDS) used energy dispersive X-ray spectroscopy (EDS) with the XFlash®6 detector series to determine the elemental composition. Using the Gemini VII 2390 V1.03 Micromeritics equipment, Brauner-Emmet-Teller (BET) analysis was used to determine the surface area and pore size of NPs. Before analysis, all samples were degassed for 12 hours at 200 °C under vacuum. Spectrums were recorded using a UV-Vis spectrophotometer (T60 Shimadzu) to determine the optical characteristics of the samples. Using a PerkinElmer Spectrum BXII Spectrophotometer set to 32 cm^{-1} scanning speed and 2.0 cm^{-1} spectral width, the powder samples were analysed using FTIR in the 400–4000 cm^{-1} range. The Raman anaysis was conducted using a High-Resolution (TE Cooled Fibre Optic) Raman System with a resolution of 4.5 cm^{-1} at 614 nm. X-ray photoelectron spectroscopy (XPS) was used to determine compositions and oxidation states using a monochromatic Al Kα1 source (1593 eV) and the Thermo Fisher Scientific K-Alpha system. A (Horiba Jovin Fluoromax 4 Spectrofluorometer) manufactured by HORIBA Scientific was utilised to get photoluminescence (PL) spectra at ambient temperature.

Photocatalytic degradation of PPs

Polyethylene (PE) was purchased from local market of Lahore, Pakistan. The LDPE was chopped into small, 3cm x 3cm pieces and about 50 mg is stored in each petri dish. A sufficient amount of dimethyl sulfoxide (DMSO) was added to petri dish, and the PEs were fully drenched in the DMSO (20 ml). A self-built photoreactor with three 150-watt metal halide lamps as the visible light source was then installed, and the petri dishes holding PEs were positioned 50 cm away from the lights. In order to achieve an equilibrium between adsorption-desorption the nanocatalysts and LDPE in the presence of DMSO, the setup was placed in a dark environment for 50 minutes. Following that, it was exposed to light continuously for 25 hours, and a little sample was taken after every 5 hours to use FTIR analysis to measure the

photodegradation of LDPE. To calculate the weight loss in percentage (wt loss %) of LDPE by produced nanocatalysts Equation 2 was used.

$$\text{wt loss } \% = \frac{(Wi - Wf)}{Wi} * 100 \quad (2)$$

Where Wi means the initial weight and Wf is the final weight (after degradation) of LDPE.

Results and Discussions

XRD

Figure 1(a) shows the XRD results for TSe0.5 and Pure TiO_2 Nanoparticles. The typical planes of (101), (004), (200), (105), (211), (116), and (220) are shown by the diffraction peaks that were seen at 2θ of 25.36◦, 38.57◦, 48.09◦, 54.97◦, 55.21◦, 62.71◦, and 68.75◦ respectively. The absence of any other peak indicated that the anatase phase was highly pure (without transitioning to the rutile phase), and the peaks and intensities that were detected matched the standard pattern card JCPDS #00-004-0836 of the anatase phase TiO_2. It is evident that, regardless of the Se/Ti ratio, neither the peak positions nor the XRD pattern altered during the doping procedure. Furthermore, the average crystallite size is 19.31nm, shown in Table 1. When compared to pure TiO_2 (22.3 nm), all of the TSe samples show an observable drop in crystallite size (20.6–19.2 nm), indicating that selenium doping might be a useful method of reducing the crystallite size of the TiO_2 photocatalyst. Variations in the lattice characteristics of the TSe sample are responsible for this decrease where, the c-axis lattice constant dropped as the selenium level increased, the a-axis lattice constant stayed constant across all TSe samples. This was explained by a change in unit cell volume caused by a slight crystal structure lattice deformation when selenium ions were added [50]. Nevertheless, the crystallite size was decreases by increasing Se concertation in TiO_2 [51].

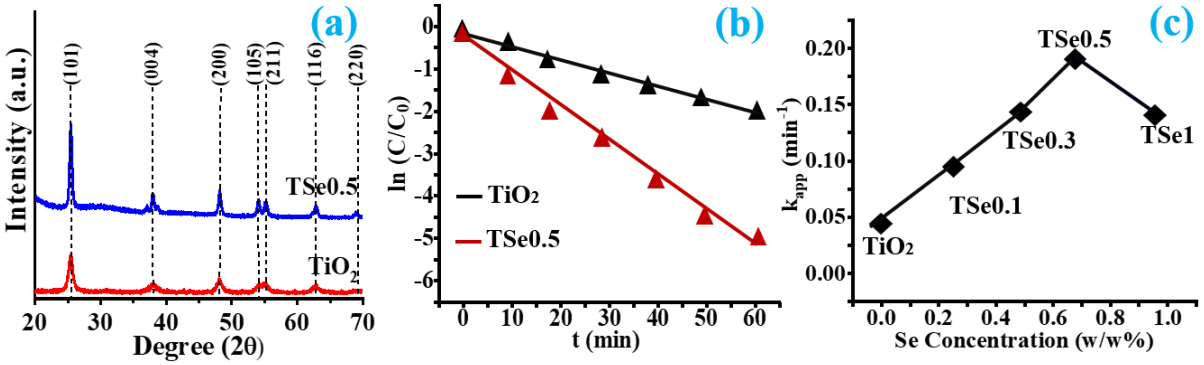

Figure 1. (a) Diffractograms of pure TiO_2 and TSe0.5, (b) first-order kinetics fitting using ln(C0/C) vs (t) and (c) the Catalytic reaction rate of each sample.

Table 1. XRD examination of the structural and microstructural characteristics of pure and TSe nanocatalysts with varying ratios.

Sample	Crystalli size (nm	FWHM(	Lattice ameters		d-spacing(
			a(Å)	c(Å)	
TiO_2	22.3	0.78	3.78	9.51	0.92
TSe0.1	20.6	0.35	3.77	9.50	0.89
TSe0.5	19.37	0.47	3.78	9.49	0.94
TSe1	19.2	0.42	3.77	9.49	0.93

SEM

SEM is used to characterise the topography of the undoped TiO_2 and TSe0.5 samples; the resulting images are displayed in Figure 2c. The TiO_2 sample is not treated in any way prior to the SEM examination. But the synthesised doped catalysts are sonicated for 10 min and then

dried before being analysed by SEM. The TiO_2 sample is made up of aggregated nanoparticles with spherical and somehow irregular morphologies as was previously seen in other studies [52]. Grain sizes range from 42.9 to 41.2 nm on average as shown in Table 2. As Se^{4+} ions enters the TiO_2 lattice, it decreases particle size because it has a smaller ionic radius than titanium. However, as the Se quantity is increased up to TSe0.5, the average size decreases notably and morphology changes from irregular forms to smooth and spherical as seen in Figure 2d. After a certain limit (>TSe0.5) increasing dopant concentration results in aggregation and agglomeration of nanocatalysts hence increasing particles size. According to Li Xueyan et al , a high surface energy was the reason behind the aggregation of this kind of particles [53]. When compared to pure nanocatalysts, the doped particles showed less agglomeration and similar results were reported by Cheng, J., et al. [54]. The lack of external contaminants in the produced samples was confirmed by the EDS analysis (Figure 2a,b), which showed the presence of Ti and O for anatase TiO_2 and Ti, O, and Se for the samples containing Se. Table S1 displays the atomic and weight percentages of the doped and TiO_2 samples.

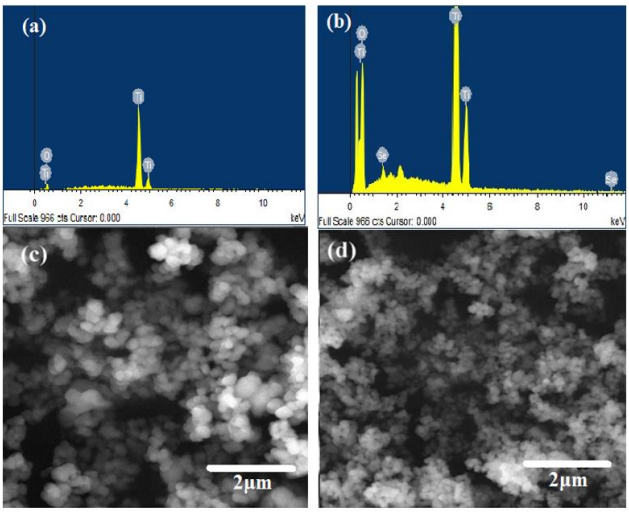

Figure 2. SEM and EDS images of TiO_2 (a, c) and TSe0.5 (b, d)

BET

The Brunauer-Emmett-Teller (BET) hypothesis is a crucial analytical technique for determining the specific surface area of a material. It aims to clarify how gas molecules physically adhere to a solid surface. The conventional IUPAC type I with a type H_2 hysteresis loop was shown by the N_2 adsorption/desorption isotherms of TiO_2 and TSe0.5 as shown in Figure 3a, b, indicating the presence of more complex mesopores that are either blocked or slightly opened. These TiO_2 samples characteristic mesoporosity is confirmed by their pore size distributions. Micropores size present in the TSe samples are given in Table 2.

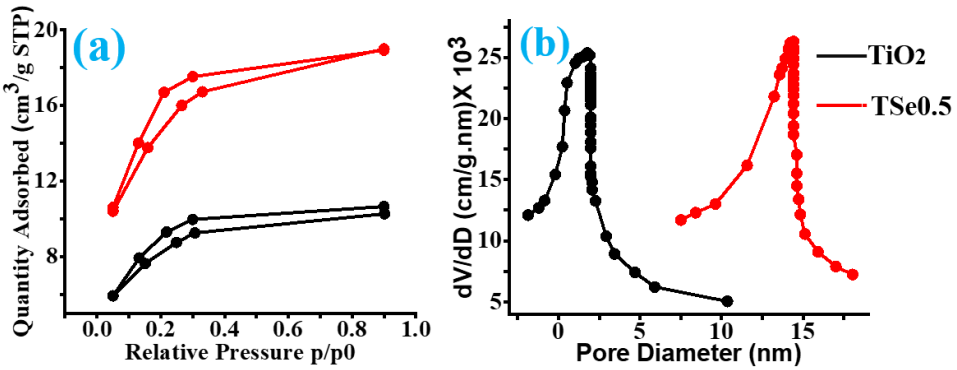

Figure 3. TiO2 and TSe0.5 nitrogen adsorption-desorption isotherms (a) and the related pore size distribution curve (b) computed in the adsorption branch of the nitrogen isotherm using the BJH equation.

Table 2. Particle size, band gap, surface area, pore size and Lagergren constant of TiO_2 and doped nanoparticles

NPs	BET surfa area (m^2/g	Bandgap (eV)	Pore diameter (n	Particle size (r	Lagergren constant $K_{deg}\times10^2$ (min^{-1})	
TiO_2	32.11	3.20	5	61.6± 0.7	2.32	0.81
TSe0.1	34.25	3.18	14.30	42.9± 1.2	2.39	0.86
TSe0.5	59.56	2.89	15.25	39.1± 7.4	2.38	0.87
TSe1	72.98	2.71	15.32	41.2± 1.3	2.41	0.88

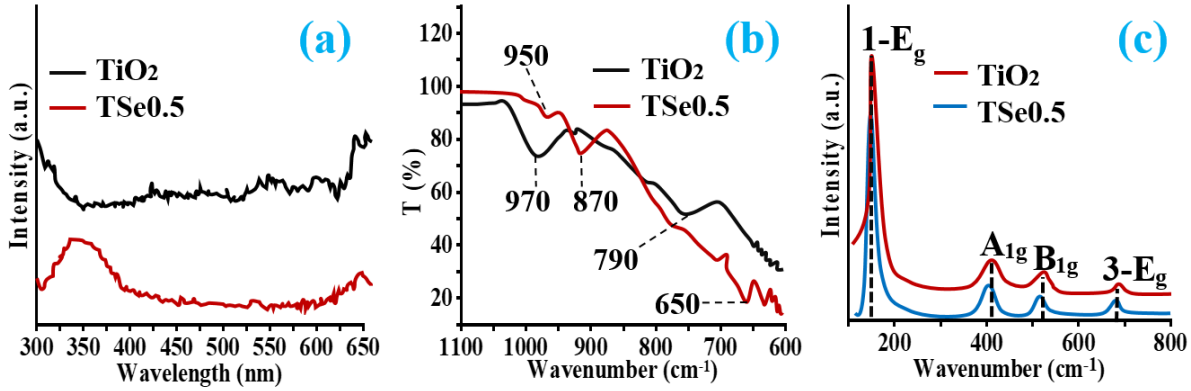

Figure 4. (a) PL spectra (b) FTIR-ATR and (c) Raman spectra of TiO2 and TSe0.5

PL spectra

PL spectra investigated destiny of electron-hole pairs in semiconductor nanocatalysts, the changes in TiO_2 surface states, and the effectiveness of charge carrier capture, displacement and transfer. A distinct, UV peak at 354 nm is visible in the PL spectrum of TSe0.5 but not for TiO_2 as shown in Figure 4a, suggesting that electron-hole recombination is much reduced in TSe0.5, possibly as a result of the high concentration of defects [55]. Additional defects are created as the Se doping concentration rises, which causes additional electron trapping. Indirect recombination via bulk defects and the surface electronic structure is the origin of another minor PL peak seen in TSe0.5 spectra at 545 nm. The formation of intermediate energy levels between valence and conduction bands may be connected to these PL peaks. These findings are consistent with XRD and BET data, which show that the optical and structural characteristics of the TSe0.5 sample are different from those of pure TiO_2 and all doped Se samples and also consistent with that of Aviles-García et al. [56], who found that TiO_2 doped with Mo and W yielded results that were similar. According to XPS, doping with an ideal concentration of Se (wt%), which takes place under two oxidation states (Se^{+4} and Se^0), has altered the optical and structural characteristics of titania. Doping Se created an acceptor level in the TiO_2 band gap by generating isolated impurity energy levels (IEL) slightly below the conduction band minimum (CBM) [57]. When subjected to irradiation light, the Se doped titania samples absorb visible light, which moves electrons from the valence band to this IEL. Additionally, they might be converted into Se0 species by being absorbed by Se^{+4} ions.

XPS

XPS was used to study the electrical structure and chemical states of TSe0.5. Figure 5a,b,c shows the Ti, O, and Se XPS spectra for TSe0.5. The stronger peaks at 458.5 eV and 464.4 eV, which correspond to Ti^{4+}, indicate that the primary valence state for Titanium in TSe is $^{+4}$. The O1s peak in Figure 5b may be attributed to two peaks, one at 531.5 eV and the other at 530.1 eV. The peak at 531.5 eV is caused by the O-H bond, while the peak at 530 is caused by the O-Ti. Due to significant lattice distortion, Se may not fill the lattice positions at greater concentrations. Electrons from neighbouring Ti and Se ions may be absorbed by O ions as the Ti-O-Se structure forms. This lowers the bonding energy as opposed to O ions, which are found at normal lattice locations.

The Se3d XPS peak, which is seen as two peaks at 58.5 eV and 55.1 eV, as shown in Figure 5c. Se^{4+} is responsible for the peak at 58.5 eV, however doping in the TiO_2 lattice environment may be the source of the much lower value. The signal at 55 eV indicates the existence of a trace amount of Se0, which may be the result of reduction from C and H in the samples and further supports the decreased chemical activity of O at such a low calcining temperature.

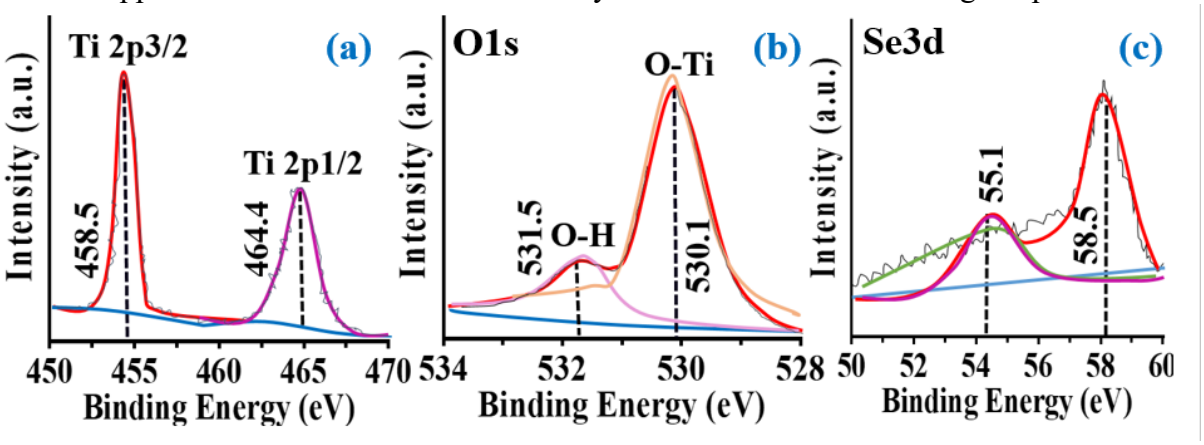

Figure 5. XPS of TSe0.5 nanoparticles

FTIR

Fourier transform infrared spectroscopy–attenuated total reflectance (FTIR–ATR) was used to identify if specific functional groups are present or absent. Previous findings indicate that the spectral region between 1000 and 600 cm^{-1} is caused by the Ti-O stretching and Ti-O-Ti bending vibrational modes in anatase [58]. As a result, we can describe the band at 970 cm^{-1} to Ti-O-Ti stretching vibrations in TiO_2 particles and the bandwidth at 790 cm^{-1} to bending vibrations.

Following doping, the Se-O bonds show stretching and bending vibrations at 650 cm^{-1} and 870 cm^{-1}, respectively, which match the vibrational characteristics of powdered selenium nanoparticles that are already reported in other studies [59]. As seen in Figure. 4b, a shift to a lower wavenumber at 945 cm^{-1} coincides with a slight decrease in the strength of Ti-O-Ti stretching vibrations.

Raman spectroscopy

An effective method for evaluating crystalline and defect structures and determining the various phases of a material is Raman spectroscopy. Figure 4c displays the Raman spectra of TSe0.5 and TiO_2. The anatase phase vibration modes for TiO_2 are displayed by peak locations at 147 cm^{-1} (1-E_g), 398 cm^{-1} ($A1_g$), 517 cm^{-1} ($B1_g$), and 689 cm^{-1} (3-E_g). XRD shows that the bands in the doped TSe0.5 sample are almost the same as those in the pure anatase phase. By usually expanding broader and moving the peak location to smaller wavenumbers, the impact of Se doping may be further assessed from shape and position. This implies that the distortion increases and the crystallite size decreases as the Se doping concentration increases.

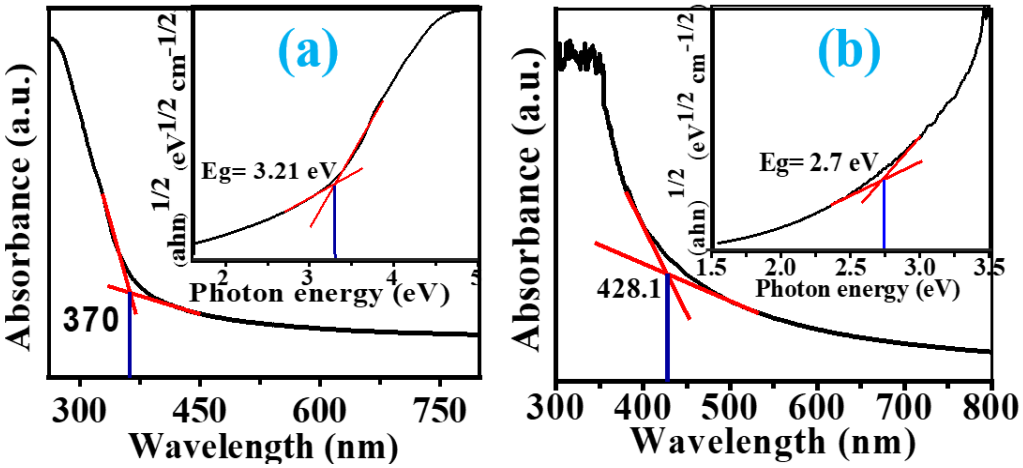

Figure 6. Absorbance and Tauc plots (inset) of a) TiO_2, b) TSe0.5.

UV-Vis spectroscopy

The optical absorption characteristics of TSe nanoparticles were examined by UV-Vis; the findings are displayed in Figure 6a, b. In the visible spectrum, TiO_2 absorption band move to a longer wavelength. The presence of $Ti^{+4,}$ which results from the high concentration of oxygen vacancies and disorder in TiO_2 at extremely low calcining temperatures, can be a reason for this bathochromic shift [60]. The TiO_2 powders show a darker pink hue with Se doping; TSe1 is the darkest shade. The highest absorption coefficient in the visible spectrum is of TSe1. TSe optical band gap was analysed using its absorption spectra. The Kubelka-Munk equation shown below as equation 3 is commonly used to describe the optical absorption close to the semiconductor band edge for indirect band gap materials such as TiO_2.

$$(\alpha h\nu)n = A(h\nu - E_g) \qquad 3$$

Where n is equal to 0.5, α is the absorption coefficient, Eg is the semiconductor band gap, hv is the photon energy, and A is a constant. The approximate values of the band gap may be determined from the tangent intercept to the X-axis, as shown in the inset of Figure 6a, b. bandgap values are displayed in Table 2. As can be observed, the least Eg of 2.71 eV is displayed by TSe1. However, TSe0.5 showed the highest photocatalytic activity (Eg = 2.77eV). There are two competing variables that might affect the final Eg of TSe1. Se doping may successfully reduce the band gap by adding additional electrical energy levels within the gap.

Degradation of PE using Se^{+4}/TiO_2

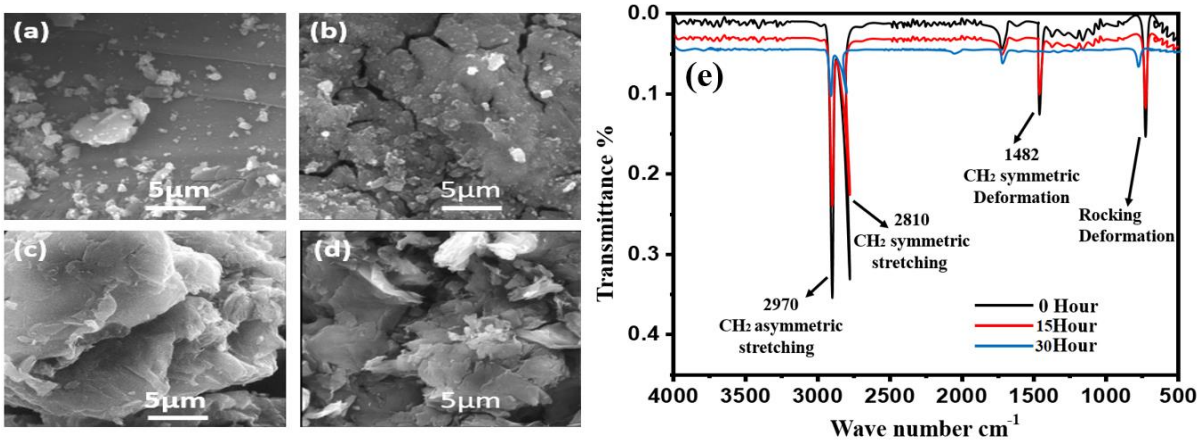

Figure 7. SEM images of PE degradation in (a) 0h (b)10h (c)20h (d)30h, (e) FTIR images of PE degradation over time

RSM graphs

Supplementary Table 2 shows the results of 20 trials (including 5 centre points) conducted for the chosen 3 independent variables at 5 levels using the BBD design. The lowest and greatest

percentages of PE that were removed were 37% and 92%, respectively. Using ANOVA, the parameter coefficients were examined as shown in Table S2. The model's variance is compared to the residual variance using the F-value. As can be seen the model's performance and significance are confirmed by the F-value of 194.92. However, the model was statistically significant if the Prob > F was less than 0.0001. Consequently, the effectiveness of photocatalytic PE removal as a function of independent parameters was predicted using a quadratic polynomial equation (Equation 4):

$$R = +89.63 - 7.13A - 1.50B + 3.12C + 7.75AB - 2.00AC - 10.25BC - 29.12A^2 - 15.87B^2 - 12.63C^2 \quad (4)$$

Here, A, B and C are coefficients of linear factors, A^2, B^2 & C^2 are coefficients of quadratic factors and AB, AC & BC are coefficients of interaction factors.
Significant effects of A (pH), B (temperature), and C (catalyst) components are also indicated by Prob > F values less than 0.05. However, the P-value for the interactions between AB, AC and BC was less than 0.05, indicating that each of them significantly affects the model

From Table S2 by elimination of insufficient factors, Eq. (4) was simplified as Eq. (5):

$$R = +89.63 - 7.13A - 1.50B + 3.12C + 7.75AB - 2.00AC - 10.25BC \quad (5)$$

Additionally, the derived model's ability to predict PE removal effectiveness was confirmed by the R^2 and R^2adj values, which were 0.9943 and 0.9892, respectively, and very near to 1. The model best fits the experimental data, as indicated by the F-value of lack of fit of 0.11, which was not significant.

Validity of the model

Validation of a model in experiment analysis requires assumptions such as the normal distribution of residuals, the variance of constant (∂2), and the independence of the residues from each other. Figure 8a shows a graph that contrasts the projected and actual values. A normal distribution of data in a straight line verifies the proper distribution of errors. The residual values are displayed against the predicted values in Figure 8b. It implies a random distribution as there are no observable patterns invariance. Furthermore, the internally analysed, Residuals plot of the model in Figure 8c shows no unusual areas. The normal distribution of the residues is confirmed by the residual normal diagram of the model in Figure 8d.

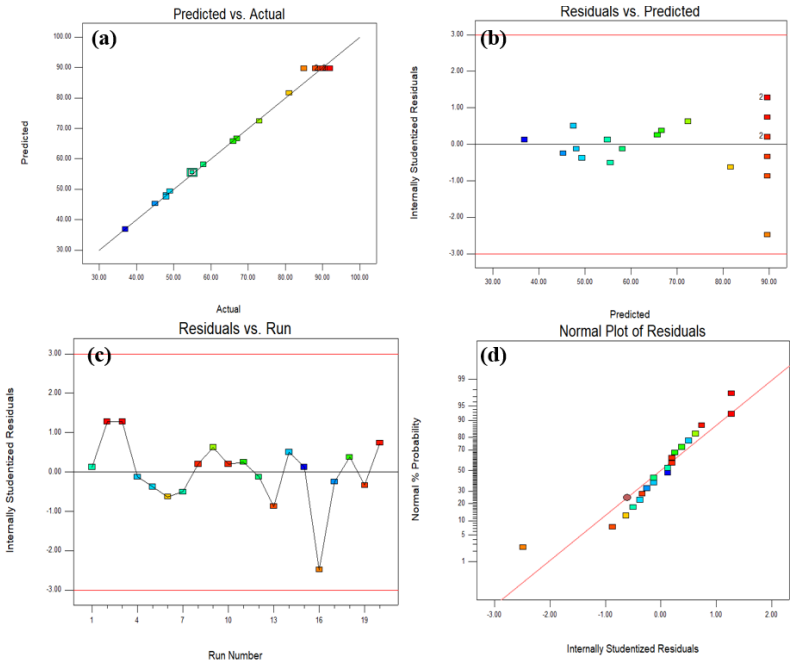

Figure 8. Statistical plots for Polyethylene removal by TSe0.5. **a**) Plots of actual values versus predicted ones. **b)** The Internally analysed residuals versus predicted ones. **c)** The Internally determined Residuals versus run number. **d)** Normal plot of residuals.

Optimization

By taking into account independent factors (changing pH, irradiation time, and photo catalyst dose) and removal efficiency as maximum utilising Design-Expert® Version 11 Software, it is possible to optimise the photocatalytic degradation conditions of PE from an economic perspective. With pH = 5.40, SeT0.5 dose = 0.5, and temperature of 45 °C, the expected PE removal was 92.10%. However, the PE removal trial result was around 90.87%, indicating an RSM performance design.

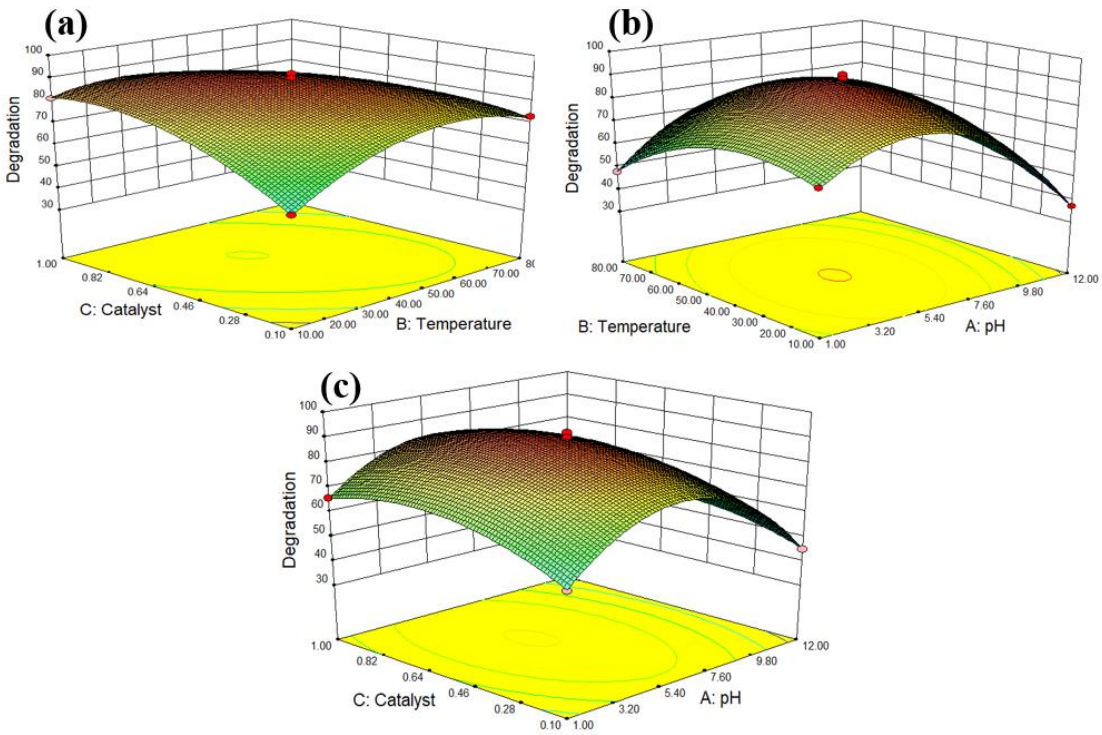

.

Figure 9. 3D plots of PE photocatalytic degradation interactions. **A)** Photocatalyst dosage vs. Temperature. **B)** Temperature vs. pH. **C)** Catalyst vs. pH.

Degradation Activity kinetics

Kinetic studies

Plotting ln(C/Co) against irradiation duration (t), under visible irradiation reveals pseudo-first-order kinetics for both doped and pure TiO_2 particles Figure 1b. The slope of the curve is used to compute the apparent response rate constant (K_{app}) As shown in Figure 1c. When Se doping is present in trace amounts, TSe0.1 exhibits a somewhat elevated K_{app} value. K_{app} steadily rises with increasing Se doping concentration, with TSe0.5 showing the greatest K_{app}. The K_{app} of TSe1 sharply drops when the Se doping concentration rises.

The powder TSe0.5 achieves the highest K_{app} value of 0.92 min^{-1}. When comparing the rate constant values under visible light irradiation, which is much greater than that of undoped TiO_2 (0.040min^{-1}). The small band gap in the visible light spectrum and the single phase (anatase), which prevent the recombination of produced electron-hole pairs, work in accordance to provide TSe0.5 superior photocatalytic performance over undoped-TiO_2.

Understanding the kinetics, mechanism, and catalytic degradation is crucial for degradation of polyethylene. Different amounts of catalyst have been used to accomplish the degradation kinetics.

$$\frac{c_T}{c_0} = \mathrm{Exp}(-k_{deg} \times t) \quad (6)$$

With a rate constant (k_{deg}), the pseudo-first-order model of Lagergren is represented by equation 6. Plotting -ln C_t/C_0 versus t enables the calculation of (k_{deg}). Figure 1b shows the photodegradation process's kinetic outcome when exposed to visible light. Table 2 provides a summary of the values of (k_{deg}) and the linear regression coefficient (r^2), which were calculated using Origin Pro software. For all pure and doped samples, the regression coefficient (r^2) is mostly more than 0.80, and the Lagergren kinetic model indicates that the kinetic rate of TSe0.5 is higher than that of undoped TiO_2.

By mixing 0.5 mg of catalyst with 10 ml of methanol, the absorbance of both pure and doped TiO_2 was measured. To get a milky suspension, the catalysts were sonicated for around half an hour. Using UV-Vis spectroscopy, the absorption was measured between 200 and 700 nm. At 387 nm, TiO_2 nanoparticles exhibit a significant absorption edge. Figure 6a, b illustrates how doping affects the light absorption properties. As stated in the literature [61], the bandgap (Eg) values are computed using the following formula and presented in Table 2 under the assumption that TiO_2 is an indirect semiconductor.

The absorbance of the doped samples is more towards red shift. As the dopant concentration increases, a significant absorption edge formed between 400 and 450 nm. Equation 7 was used to create tauc plots using absorbance data.

$$E=hc/\lambda \quad (7)$$

As 1 eV= 1.60×10^{-19} J

hc = $(6.62 \times 10^{-34}$ Js). $(3 \times 10^8$ m/s)

= 6.62×10^{-34}. (1.6×10^{-19}) $(3 \times 10^8$ m/s)

= 1.24 eV x 10 -6 = 1240 V (nm)

=1240/λ = band gap in eV

Dopants provide internal band gaps that lower the rate of recombination, as can be seen from the redshift. They function as electron traps because Se exists on its own as Se^{+4}. It is evident from the photocatalyst process that Se^{+4} decreases the rate of electron and hole recombination by capturing electrons from conduction band of TiO_2. By absorbing visible light, the valence band electron of Se-TiO_2 may easily go to the CB, causing holes in the VB.

These photogenerated electrons are scavenged by the oxygen molecules absorbed on the surface of the photocatalyst, producing very reactive superoxide anion radicals that, according to scavenging experiments, are essential to the photodegradation of the contaminants. Likewise, the photogenerated holes in the VB of TiO_2 readily transform H_2O and OH^- into hydroxyl ($^{\bullet}OH$) radicals. This significantly speeds up the photodegradation of polyethylene. Thus, hydroxyl ($^{\bullet}OH$) and superoxide ($^{\bullet}O^{2-}$) radicals are the ROS species on the photocatalyst.

Se-TiO_2 + hν ⟶ Se-TiO_2 (eCB^- + hVB^+)

Se-TiO_2 (ECB^-) +O_2 ⟶ Se-TiO_2 + $^{\bullet}O_2$

Se-TiO_2 (hVB^+) +H_2O ⟶ Se-TiO_2 + $^{\bullet}OH$ +H^+

$^{\bullet}$Se-TiO_2 + OH^- ⟶ Se-TiO_2 + $^{\bullet}OH$

PE +$^{\bullet}O_2$ + $^{\bullet}OH$ ⟶ Degradation products

Effect of Se-doping Concentration

Polyethylene is photocatalytically broken down in an aqueous solution by pure and TSe0.5 nanopowders, respectively, when exposed to visible light. All nanocatalysts exhibit continuous degradation of polyethylene during the course of irradiation as shown in Figure 7, The TSe0.5 catalyst outperforms all other Se-doped nanocatalysts in terms of degrading efficiency throughout all time periods, as well as pure TiO_2. After 30 hours of irradiation, the

photocatalytic degradation efficiency of TSe0.5 reaches around 91.4% for PE of the original concentration. These findings suggest that Se doping can enhance the photocatalysis process even at low loading levels. For the purpose of effectively enhancing the photocatalytic activity of TiO_2, TSe0.5 is the ideal metal concentration. However, the degrading activity falls when the Se content rises to 1%. This may be because (i) too much selenium covers the catalyst's surface active sites and (ii) the combination of the charge carriers speeds up photocatalytic degradation with a higher Se charge, this finding may indicate that a higher selenium content will decrease the catalytic photodegradation capacity [61]. Similar results were obtained by Cheng et al. They demonstrated that either too high or too low doping of TiO_2 causes noticeable carrier recombination or inefficient visible light absorption. Their results indicate that the presence of fewer metal ions reduces the recombination rate because the excited electrons are more effectively contained [62]. However, when the dopant amount is relatively big, the metal ions become recombination sites for positive holes due to their negative charge from the electrons, which reduces the photocatalytic activity.

Weight loss analysis

Weight loss analysis of PE films were done by obtaining remains of PE from Nanoparticles liquid mixer, subsequently treated with chloroform, and washed with 2% sodium dodecyl sulfate (SDS) for 4 hours and distilled water for 10 minutes to remove nanoparticles residues on the surface. The washed LDPE was then placed on a filter paper and dried at 60 °C for 24 hours prior weighing. The percentage weight loss of the LDPE was determined as done before [63] by using this formula shown in equation 8.

Weight loss (%) = [(Initial weight – Final weight)/Initial weight] x 100. (8)

Time (h)	TiO_2	TSe0.5
0	100	100
5	98	82
10	97	71
15	91	59
20	82	44
25	80	23
30	79	11

Table 3. Weight loss analysis

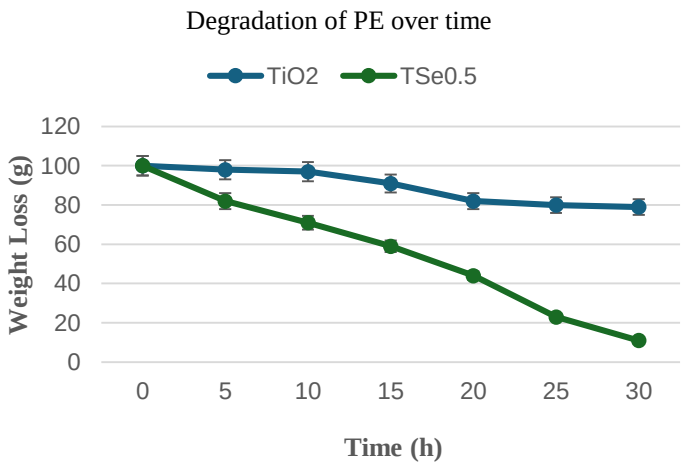

Figure 10. Degradation efficiency of TSe0.5 and pure TiO_2

Proposed Photocatalytic Mechanism

This section describes how the development of the photo-induced charge transporters between Se and TiO_2 has been successfully assessed using Mulliken electronegativity theory. This concept describes the operation of heterojunctions in Anderson's model. The semiconductors' Mulliken-electronegativity, ECB and EVB, are the conduction and valence band edge potentials, respectively, whereas the bandgap of the semiconductors Eg and Ee is the free energy of electrons on the H_2 (4.5 eV) for Se and TiO_2. The conduction band edge of Se and TiO_2 is negative with regard to the hydrogen reduction potential on the standard hydrogen electrode scale. Likewise, the positive valence band edge of TiO_2 is greater than that of Se.

Both semiconductors will collect, be led from the TiO_2 surface to the Se surface, and be exposed to the visible spectrum (400 nm) under an internal electric field at either side of the junction. They have different electronegativities and band positions. The photogenerated electrons will go from TiO_2 to Se^{+4}, and the photogenerated holes will push their way from the valence bands of Se^{+4} to the valence bands of TiO_2 under the influence of an inner electric field. By effectively separating and mobilising the photogenerated electrons and holes, these processes increase the Se-TiO_2 photocatalysts' photocatalytic activity. By producing hydrogen through photo-induced water breakdown, the photo-removal process of dyes offers a straightforward solution to both energy and environmental problems.

Efficient separation of electron–hole pairs in the excited TiO_2 may promote an efficient transition into photoinduced electrons between TiO_2 and Se. This drastic splitting action is a crucial step in the colour removal process. The effectiveness of the photo-reaction is largely dependent on how well photo-generated electron-hole pairs are divided and how well unprocessed organic contaminants are adsorbed on the photocatalysts. The holes may react or be absorbed via the surface hydroxyl to produce hydroxyl radicals. Dye molecules were able to move from single elucidation to the interface due to the disruption of the adsorption equilibrium, where they were then broken down into CO_2, H_2O, and other raw materials by redox reactions.

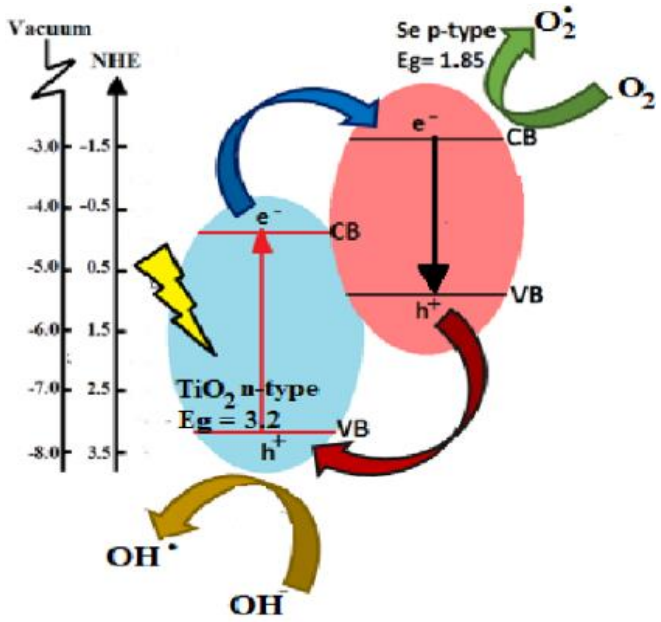

Figure 11. Proposed mechanism

Usability and stability of the photocatalyst

For long-term uses, the photocatalyst's stability and usefulness are crucial. Centrifugation is used to recover the photocatalyst particles, which are then gathered for further cycles. For 10 PE degrading cycles (20 mg L−1), the reusable performance of TSe0.5 was examined

(Supplementary Fig. 3). The photocatalytic activity of TSe0.5 dropped from 89.87% to 52.76% during 10 cycles. The causes for this decline in photocatalytic activity are as follows: (1) During the recovery step (washing and drying), some photocatalyst may be lost, which lowers the surface catalytic activity and subsequent cycle efficiency. (2) As a result of PE and its intermediates degradation which block pores and active sites, the photocatalyst's catalytic surface activity progressively declined following each cycle.

Conclusion

In summary, the sol-gel method was adopted to synthesize pure and Se-doped TiO_2 nanoparticles by varying Se content. XRD results show that all the peaks are attributed to pure anatase tetragonal having different crystallite sizes ranging from 20.6-21.2 nm. The crystallite size decreases as the dopant concentration increases. SEM analysis showed the morphology of TiO_2 as irregular but doping causes a change in morphology as it becomes spherical and increased dopant causes aggregated plates. Loading more dopants also increases the surface area of particles. TSe0.5 has the highest surface area (59.56 m^2/g) and high degradation rate probably because of the smaller size and well-dispersed particles. However, dopant up to 1% cause agglomeration on the surface and therefore lowering the photocatalytic activity and stability. TSe0.5 loading has an optimum substitution of Ti^{4+} and Se^{+4} within the lattice of TiO_2. This leads to a charge balance deficit and thus an oxygen defect, and made an acceptor level in the band gap of TiO_2 by generating isolated impurity levels of energy just below the conduction band of TiO_2.degradation activity was measured on polyethylene plastic bags. Samples were collected at regular intervals and examined using SEM and FTIR which shows a significant weight loss and degradation of PE samples.

Declaration of Competing Interest

The authors declare that they have no known competing financial interests or personal relationships that could have appeared to influence the work reported in this paper.

Acknowledgements

We would like to thank the research committee of National University of science and Technology (NUST) and Minhaj University Lahore for supporting this work.

References

Huang, D., et al., Degradation of polyethylene plastic in soil and effects on microbial community composition. Journal of Hazardous Materials, 2021. **416**: p. 126173.

Bouchet, j.B.M.Z.X.L.A.K.G.B.P.P.A., National Guidance for Plastic Pollution Hotspotting and Shaping Action. 2020.

Olatunji, O., A History of Plastics, in Re-envisioning Plastics Role in the Global Society: Perspectives on Food, Urbanization, and Environment, O. Olatunji, Editor. 2024, Springer Nature Switzerland: Cham. p. 11-26.

Aphrodite, L.M.i.C.A.C.P.L.A.M.A.D.R. and S.S.S.E. Tonda., Turning off the Tap How the world can end plastic pollution and create a circular economy. 2023.

Nayanathara Thathsarani Pilapitiya, P.G.C. and A.S. Ratnayake, The world of plastic waste: A review. Cleaner Materials, 2024. **11**: p. 100220.

Shahul Hamid, F., et al., Worldwide distribution and abundance of microplastic: How dire is the situation? Waste Management & Research, 2018. **36**(10): p. 873-897.

Maquart, P.-O., Y. Froehlich, and S. Boyer, Plastic pollution and infectious diseases. The Lancet Planetary Health, 2022. **6**(10): p. e842-e845.

Beloe, C.J., M.A. Browne, and E.L. Johnston, Plastic debris as a vector for bacterial disease: an interdisciplinary systematic review. Environmental Science & Technology, 2022. **56**(5): p. 2950-2958.

Lind, L. and P.M. Lind, Can persistent organic pollutants and plastic-associated chemicals cause cardiovascular disease? Journal of internal medicine, 2012. **271**(6): p. 537-553.

Vasse, G.F. and B.N. Melgert, Microplastic and plastic pollution: impact on respiratory disease and health. European Respiratory Review, 2024. **33**(172).

Lamb, J.B., et al., Plastic waste associated with disease on coral reefs. Science, 2018. **359**(6374): p. 460-462.

Bruno, A., et al., Orally Ingested Micro-and Nano-Plastics: A Hidden Driver of Inflammatory Bowel Disease and Colorectal Cancer. Cancers, 2024. **16**(17): p. 3079.

Rahimi, A. and J.M. García, Chemical recycling of waste plastics for new materials production. Nature Reviews Chemistry, 2017. **1**(6): p. 0046.

Paço, A., et al., Biodegradation of polyethylene microplastics by the marine fungus Zalerion maritimum. Science of the Total Environment, 2017. **586**: p. 10-15.

Plomer, J.J. and T. Traugott, New High Heat Stable, Low Gloss. Automotive Interior Trim Resins Having Excellent Processability, 1989, SAE Technical Paper.

Jeyavani, J., et al., A convenient strategy for mitigating microplastics in wastewater treatment using natural light and ZnO nanoparticles as photocatalysts: A mechanistic study. Journal of Contaminant Hydrology, 2024. **267**: p. 104436.

Zhou, D., et al., Efficient photocatalytic degradation of the persistent PET fiber-based microplastics over Pt nanoparticles decorated N-doped TiO2 nanoflowers. Advanced Fiber Materials, 2022. **4**(5): p. 1094-1107.

Villarreal-Morales, R., et al., Enhanced performance of TiO2 doped with aluminum for the photocatalytic degradation of a mixture of plasticizers. Journal of Environmental Chemical Engineering, 2022. **10**(1): p. 107100.

Rani, M. and U. Shanker, Efficient removal of plastic additives by sunlight active titanium dioxide decorated Cd–Mg ferrite nanocomposite: Green synthesis, kinetics and photoactivity. Chemosphere, 2022. **290**: p. 133307.

Pham, T.H., et al., Removal of bisphenol A micropollutants released from plastic waste using Pt-ZnO photocatalyst. Environmental Geochemistry and Health, 2024. **46**(9): p. 335.

Edirisooriya, E.T., et al., Photo-reforming and degradation of waste plastics under UV and visible light for H2 production using nanocomposite photocatalysts. Journal of Environmental Chemical Engineering, 2023. **11**(2): p. 109580.

Lian, J.-j., et al., Adsorption mechanism and influencing factors of selenium under the coexistence of nanoparticles and microplastics. Desalination and Water Treatment, 2024. **318**: p. 100338.

Ngan, A., Practical Systems for Photocatalytic Selenium Reduction and Removal: Shining Light on Sustainable Industrial Water Management, 2024, University of Toronto (Canada).

Ostovar, M., N. Saberi, and R. Ghiassi, Selenium contamination in water; analytical and removal methods: a comprehensive review. Separation Science and Technology, 2022. **57**(15): p. 2500-2520.

Ran, M., et al., Efficient removal of Sb (III) from wastewater using selenium nanoparticles synthesized by Psidium guajava plant extract. Environmental Science and Pollution Research, 2024. **31**(31): p. 43781-43797.

Mbonyiryivuze, A., et al., Titanium dioxide nanoparticles biosynthesis for dye sensitized solar cells application. 2015.

Das, A., et al., Wastewater treatment with the advent of TiO2 endowed photocatalysts and their reaction kinetics with scavenger effect. Journal of Molecular Liquids, 2021. **338**: p. 116479.

Ghamarpoor, R., A. Fallah, and M. Jamshidi, A review of synthesis methods, modifications, and mechanisms of ZnO/TiO2-based photocatalysts for photodegradation of contaminants. ACS omega, 2024. **9**(24): p. 25457-25492.

Yuwendi, Y., et al., Photocatalytic degradation of polyethylene microplastics and disinfection of E. coli in water over Fe-and Ag-modified TiO2 nanotubes. Bulletin of Chemical Reaction Engineering & Catalysis, 2022. **17**(2): p. 263-277.

Hasanuzzaman, M., et al., Co-doped (N and Fe) TiO2 photosensitising nanoparticles and their applications: a review. Advances in Materials and Processing Technologies, 2024. **10**(3): p. 1320-1343.

Piątkowska, A., et al., C-, N-and S-doped TiO2 photocatalysts: a review. Catalysts, 2021. **11**(1): p. 144.

Mousa, M.A., et al., Mangrove leaves aqueous extract mediated green synthesis of C-doped TiO2 nanoparticles and their ecotoxic effect on rotifers. International Journal of Nano and Material Sciences, 2018. **7**(1): p. 16-30.

Abdelraheem, W.H., et al., Hydrothermal synthesis of photoactive nitrogen-and boron-codoped TiO2 nanoparticles for the treatment of bisphenol A in wastewater: Synthesis, photocatalytic activity, degradation byproducts and reaction pathways. Applied Catalysis B: Environmental, 2019. **241**: p. 598-611.

Ariza-Tarazona, M.C., et al., Low environmental impact remediation of microplastics: Visible-light photocatalytic degradation of PET microplastics using bio-inspired C, N-TiO2/SiO2 photocatalysts. Marine Pollution Bulletin, 2023. **193**: p. 115206.

Cong, Y., et al., Synthesis and Characterization of Nitrogen-Doped TiO2 Nanophotocatalyst with High Visible Light Activity. The Journal of Physical Chemistry C, 2007. **111**(19): p. 6976-6982.

Wang, J., et al., Origin of Photocatalytic Activity of Nitrogen-Doped TiO2 Nanobelts. Journal of the American Chemical Society, 2009. **131**(34): p. 12290-12297.

Slimani, Y., et al., Synthesis of Ce and Sm Co-doped TiO2 nanoparticles with enhanced photocatalytic activity for rhodamine B dye degradation. Catalysts, 2023. **13**(4): p. 668.

Kuo, C.-Y., H.-K. Jheng, and S.-E. Syu, Effect of non-metal doping on the photocatalytic activity of titanium dioxide on the photodegradation of aqueous bisphenol A. Environmental technology, 2021. **42**(10): p. 1603-1611.

Zatirostami, A., A dramatic improvement in the efficiency of TiO2-based DSSCs by simultaneous incorporation of Cu and Se into its lattice. Optical Materials, 2021. **117**: p. 111110.

Song, W., et al., An efficient Se-doping strategy to boost sodium storage capacity of anatase TiO2 nanospheres. Scripta Materialia, 2022. **215**: p. 114705.

Athira, K., et al., Synthesis and characterization of Mg doped TiO2 nanoparticles for photocatalytic applications. Materials Today: Proceedings, 2020. **33**: p. 2321-2327.

Shenoy, R.U.K., et al., The purview of doped nanoparticles: Insights into their biomedical applications. OpenNano, 2022. **8**: p. 100070.

Fuziki, M., et al., Sol–Gel Fe/TiO 2 Magnetic Catalysts Applied to Selenium Photoreduction. Topics in Catalysis, 2020. **63**: p. 1131-1144.

Hadjez, F., et al., Se (IV)-Doped Monodisperse Spherical TiO 2 Nanoparticles for Adhesively Bonded Joint Reinforcing: Synthesis and Characterization. SAE International Journal of Materials and Manufacturing, 2024. **17**(05-17-03-0017).

Tsotetsi, D., M. Dhlamini, and P. Mbule, Sol-gel synthesis and characterization of Ho3+ doped TiO2 nanoparticles: Evaluation of absorption efficiency and electrical conductivity for possible application in perovskite solar cells. Optical Materials, 2022. **130**: p. 112569.

Muzakkar, M., et al. Chalcogenide material as high photoelectrochemical performance Se doped TiO2/Ti electrode: Its application for Rhodamine B degradation. in Journal of Physics: Conference Series. 2019. IOP Publishing.

Mathew, S., et al., Effect of chalcogens (S, Se, and Te) on the anatase phase stability and photocatalytic antimicrobial activity of TiO2. Materials Today: Proceedings, 2020. **33**: p. 2458-2464.

Yueyu, S., The synergistic degradation of pollutants in water by photocatalysis and PMS activation. Water Environment Research, 2023. **95**(10): p. e10927.

Xie, W., R. Li, and Q. Xu, Enhanced photocatalytic activity of Se-doped TiO2 under visible light irradiation. Scientific reports, 2018. **8**(1): p. 8752.

Galeano, L., et al., Dry-co-grinding of doped TiO2 with nitrogen, silicon or selenium for enhanced photocatalytic activity under UV/visible and visible light irradiation for environmental applications. Materials Science in Semiconductor Processing, 2019. **91**: p. 47-57.

Fuziki, M., et al., Effects of synthesis parameters on the properties and photocatalytic activity of the magnetic catalyst TiO2/CoFe2O4 applied to selenium photoreduction. Journal of Water Process Engineering, 2021. **42**: p. 102163.

Karthikeyan, C., et al., Recent advances in semiconductor metal oxides with enhanced methods for solar photocatalytic applications. Journal of alloys and compounds, 2020. **828**: p. 154281.

Liu, D., et al., Fe-functionalized α-Fe2O3/ZnO nanocages for ppb-level acetone gas sensing. ACS Applied Nano Materials, 2022. **5**(4): p. 5745-5755.

Cheng, H., et al., Selenium-modified TiO2 nanoarrays with antibacterial and anticancer properties for postoperation therapy applications. ACS Applied Bio Materials, 2018. **1**(5): p. 1656-1666.

Nematollahi, R., et al., Experimental and theoretical studies on the synergistic effect of P and Se co-doped g-C3N4 loaded with Ag nanoparticles as an affective photocatalyst under visible light irradiation. Journal of Molecular Liquids, 2023. **369**: p. 120387.

Avilés-García, O., et al., Removal of metoprolol by means of photo-oxidation processes. Catalysis Today, 2022. **397**: p. 562-573.

Sun, M., et al., Donor-acceptor codoping effects on tuned visible light response of TiO2. Journal of Environmental Chemical Engineering, 2020. **8**(5): p. 104168.

Abbas, M. and M. Rasheed. Solid state reaction synthesis and characterization of Cu doped TiO2 nanomaterials. in Journal of Physics: Conference Series. 2021. IOP Publishing.

Komaraiah, D., et al., Structural, optical and photoluminescence studies of sol-gel synthesized pure and iron doped TiO2 photocatalysts. Ceramics International, 2019. **45**(18): p. 25060-25068.

Muzakkar, M.Z., et al. Performance of selenium doped TiO2/Ti composite electrodes (Se-TiO2/Ti): Photoelectrocatalyst of reactive green 19 under UV-Visible irradiation. in AIP Conference Proceedings. 2022. AIP Publishing.

Geldasa, F.T., et al., Density functional theory study of Chlorine, Fluorine, Nitrogen, and Sulfur doped rutile TiO2 for photocatalytic application. Scientific Reports, 2025. **15**(1): p. 3390.

Zhu, Y., et al., Engineering the Metal/Oxide Interfacial O-Filling Effect to Tailor Oxygen Spillover for Efficient Acidic Water Oxidation. Advanced Functional Materials, 2025: p. 2421354.

Shilpa, S., N. Basak, and S.S. Meena, Transcriptomics-Driven Analysis of LDPE Degradation by Pseudomonas Aeruginosa WD4 Isolated from Plastic Waste Dumpsite. Indian Journal of Microbiology, 2025: p. 1-12.